

Kilonova Light Curve Parameter Estimation Using Likelihood-Free Inference

M. M. Desai,^{1,2*} D. Chatterjee,^{1,2} S. Jhavar,⁵ P. Harris,³ E. Katsavounidis^{1,2} and M. W. Coughlin⁴

¹ MIT Kavli Institute, 70 Vassar St, Cambridge, MA 02139, USA

² MIT LIGO Laboratory, MIT, 185 Albany St, NW22, Cambridge, MA 02139, USA

³ Laboratory for Nuclear Science, MIT, 185 Albany St, 24, Cambridge, MA 02139, USA

⁴ School of Physics and Astronomy, University of Minnesota, 116 Church St SE, Minneapolis, MN 55455, USA

⁵ Institut für Physik und Astronomie, Universität Potsdam, Haus 28, Karl-Liebknecht-Str. 24/25, 14476, Potsdam, Germany

Accepted XXX. Received YYY; in original form ZZZ

ABSTRACT

We present a parameter estimation algorithm on kilonova light curves using likelihood-free inference. Our inference is optimized through a pre-trained embedding network that marginalizes the time of arrival and the luminosity distance of the signal. We find that parameter inference utilizing a pre-trained embedding outperforms the use of likelihood-free inference alone, reducing training time and offering the capability to marginalize over certain nuisance parameters. The model is capable of retrieving the intrinsic parameters of the kilonova light curves with a comparable accuracy and precision to nested sampling methods while taking significantly less computational time. This framework has been integrated into the publicly available Nuclear Multi-Messenger Astronomy codebase so users can leverage the model for their inference purposes. This algorithm is broadly applicable to parameterized or simulated light curves of other transient objects.

Key words: neutron star mergers – methods: numerical – stars: neutron

1 INTRODUCTION

For several decades, the mergers of compact binaries made up of two neutron stars (BNS), or a neutron star with a black hole (NSBH), have been theorized to emit a sufficient amount of neutron star ejecta to supply heavy elements through a process known as rapid nucleosynthesis, commonly referred to as the r-process (Lattimer & Schramm 1974; Eichler et al. 1989; Freiburghaus et al. 1999). With the observation of the well-studied kilonova AT2017gfo (Tanvir et al. 2017) and the associated gravitational wave GW170817 and gamma ray burst GRB170817A (Abbott et al. 2017), recent research has been done on estimating the properties of the neutron star ejecta (Kasen et al. 2017; Bulla 2023). This has led to developments in understanding the properties and equation of state of neutron stars (Radice et al. 2018; Mathias et al. 2024), additional measurements of the Hubble constant (Bulla et al. 2022), and investigating the contributions of these mergers to heavy element production via the r-process (Siegel 2019).

Current operational detectors such as the Zwicky Transient Facility (ZTF, Bellm et al. (2018)) and the Wide-Field Infrared Transient Explorer (WINTER, Frostig et al. (2022)) are optimized to target electromagnetic (EM) counterparts to gravitational waves. Additionally, the upcoming Vera C. Rubin Observatory (previously referred to as Large Synoptic Survey Telescope, LSST) will have the opportunity to detect kilonovae signals (Ivezic et al. 2019; Cowperthwaite et al. 2019; Andreoni et al. 2019, 2022, 2024). Improvements to current

gravitational-wave detectors and plans to construct next-generation detectors are expected to lead to an increase in known BNS/NSBH events and lead to an order of 10 new kilonova observations per year with the Vera C. Rubin Observatory and the Nancy Grace Roman Space Telescope (Gupta et al. 2023).

In anticipation of these events, an effort is being made to create models to simulate potential light curves. The first simple kilonova model was developed by Li & Paczyński (1998), which assumed an adiabatically expanding spherically symmetric envelope. Solutions to their equations provided an estimate of the luminosity and duration of a kilonova. Subsequently, the observation of GW170917 led to a two-part framework: an initial lanthanide-poor blue emission, and a secondary lanthanide-rich red emission (Metzger 2017). Several models have been developed to understand various aspects of kilonova (Kasen et al. 2017; Dietrich et al. 2020; Anand et al. 2021; Zhu et al. 2021; Anand et al. 2023; Wollaeger et al. 2021; Kedia et al. 2023; Gompertz et al. 2023), some of which are derived utilizing the three-dimensional Monte Carlo radiation transport modelling code POSSIS (Bulla 2019). To consolidate these models, a nuclear multi-messenger astronomy package referred to as NMMA offers tools to generate light curves from several models and perform parameter estimation on these simulated events (Pang et al. 2023). We choose the spectral energy distribution (SED) model grid from Kasen et al. (2017), hereby referred to as Ka2017, for our light curve generation through NMMA. The implementation of this model is further discussed in Section 2.

Over the past few years, developments in machine learning (ML) techniques have explored various avenues in reducing the compu-

* E-mail: mmdesai@mit.edu (MIT)

tational cost and time for studying light curves. While ML-based improvements have been made in the vitesse of light curve generation using variational autoencoders (Saha et al. 2024) and neural networks (Peng et al. 2024), parameter estimation of this data remains an untapped field. One disadvantage of sampling methods is that the likelihood calculation of $p(d|\theta)$ at each inference step is computationally expensive. To avoid this calculation, likelihood-free or simulation-based inference (LFI/SBI) offers a potential alternative method (see Cranmer et al. (2020) for a review).

In this paper, we describe our framework for faster parameter inference using LFI with comparable accuracy and precision to nested sampling (Skilling 2006). We simulate light curves using the Ka2017 model grid and ZTF noise realizations. We use an embedding neural network for the light curves to marginalize over the distance to the source and the exact peak time over a data segment. This allows us to focus on the intrinsic parameters of the light curve such as M_{ej} , V_{ej} , and X_{lan} , which are further described in Section 2. This is achieved by creating alternate, or shifted, views of each light curve with the same intrinsic parameters, while varying the time and luminosity distance. These views are jointly embedded by minimizing the variance, invariance, and covariance of the two data views. Conditioned on this data summary, a normalizing flow is used to infer these kilonova parameters on a logarithmic scale: $\log_{10}(M_{ej}/M_{\odot})$, $\log_{10}(V_{ej}/c)$, and $\log_{10}(X_{lan})$. We compare our posterior distributions to nested sampling results produced with the PyMultiNest package (Feroz et al. 2009). We explain our selection of model and priors for the data in Section 2. Section 3 details the ML architecture and demonstrates its efficacy on simulated kilonova light curves, with the results provided in Section 4.

2 DATA

In this section, we discuss prior selection and data preparation for the ML model. We simulate light curve data using the Ka2017 hydrodynamical grids, which are available through the NMMA package (Kasen et al. 2017; Pang et al. 2024). We focus on obtaining realistic light curves viewable from ZTF, thereby simulating data in all three of its bands: `ztfg`, `ztfr`, and `ztfi`.

The composition and appearance of a kilonova is controlled by the spectral energy distribution (SED). The Ka2017 model parametrizes this SED through the combined dynamical and disk mass (M_{ej}), velocity (V_{ej}), and lanthanide fraction (X_{lan}) of the ejecta. Lanthanide fraction, X_{lan} , can serve as a metric for heavy r-process matter, as lanthanides contribute anywhere from 1 to 10 % of the total ejecta mass (Kasen et al. 2017). The line transitions from lanthanides greatly increases the opacity, resulting in long diffusion times and longer light curves. The Ka2017 model accounts for two kilonova mass ejection methods: a brief stripping of the stars due to tidal forces ($10^{-3}M_{\odot} < M_{ej} < 10^{-2}M_{\odot}$), and a secondary ejection of mass from the accretion disk blown by neutrino-driven winds ($10^{-2}M_{\odot} < M_{ej} < 10^{-1}M_{\odot}$) (Martin et al. 2015). The initial shock occurs at high speeds on the order of a dynamical velocity $V_{dyn} \sim 0.2c - 0.3c$, while the disk mass disperses at rates of $V_{disk} \sim 0.05c - 0.1c$. These quantities also affect the peak of the light curve, with large ejecta mass and velocity producing brighter and longer lasting kilonova signals. Ka2017 combines these quantities as the ejecta parameters M_{ej} and V_{ej} , which we use to parametrize our model. In this study, we neglect the effects of host galaxy and Milky Way extinction effects on the light curve.

To ensure that light curves are visible by ZTF, we selected broad parameter ranges that were capable of producing detections in addi-

Table 1. Prior boundaries for data generation.

Parameter	Minimum	Maximum
$\log_{10}(M_{ej}/M_{\odot})$	-1.9	-1
$\log_{10}(V_{ej}/c)$	-1.52	-0.53
$\log_{10}(X_{lan})$	-9	-3
t (s)	-2	6
d_L (Mpc)	50	200

tion to the considerations provided by Kasen et al. (2017). These priors are detailed in Table 1. We choose time and luminosity distance, (t , d_L), as our nuisance parameters that we wish to marginalize. Our time prior is selected to create a conservative variability for where the light curve peaks. Our distance prior allows our model to be sensitive to the edge of EM detectability with ZTF and the expected two detector LIGO O4 BNS inspiral range of 25-130 Mpc (Abbott et al. 2018). While GW170817 was detected at 40 Mpc, optical surveys are expected to be sensitive to kilonovae at a distance of up to 200 Mpc with a limiting magnitude of 22 mag (Sagués Carracedo et al. 2021).

Our data is simulated at a regular cadence of one detection every six hours over a 20 day period of time. While this is an optimistic detection scheme, we discuss potential relaxation schemes in Section 4. We sample uniformly from our intrinsic parameters $\log_{10}(M_{ej}/M_{\odot})$, $\log_{10}(V_{ej}/c)$, and $\log_{10}(X_{lan})$, and our extrinsic parameters t and d_L . In the case where the light curve is dim or short-lived, non-detections are encoded as the magnitude detection limit of 22.0 in all bands. This is a typical conservative restriction given that ZTF is limited to 20.8, 20.6, and 19.9 mag [21.6, 21.4, and 21.9 mag] for the g, r, and i bands for a 30s [300s] exposure time (Bellm et al. 2019; Almualla et al. 2021). Since the broad priors produce both extremely short and long light curves, we pad the data with our non-detection limit in order to maintain a standard length of data for our model. For training purposes, a minimum amount of 8 cumulative detections in any of the three bands is set as a requirement.

To train the network, we create a set of “fixed” data, d , which share the same initial arrival time $t = 0$ and a luminosity distance of $d_L = 50$ Mpc. For each fixed light curve, an alternative “shifted” light curve d' is generated by modifying t and d_L in accordance with the priors in Table 1. A single fixed light curve will have its shifted counterpart that shares the precise values for $\log_{10}(M_{ej}/M_{\odot})$, $\log_{10}(V_{ej}/c)$, and $\log_{10}(X_{lan})$, resulting in the same physical phenomena but a different observed light curve. In this way, two views of data generated by the same intrinsic parameters are created. Additionally, each light curve is simulated with unique instrument noise to ensure that all views of the same intrinsic parameters are distinct. We utilize both views to train our data summary, and the shifted view to train our normalizing flow.

3 METHOD

In this section, we present our ML-based framework for parameter estimation using LFI. We introduce the concept of an embedding network that permits the marginalization of certain parameters and reduces the size of the following inference network in Section 3.1. We then use normalizing flows to perform parameter inference, which is described in Section 3.2.

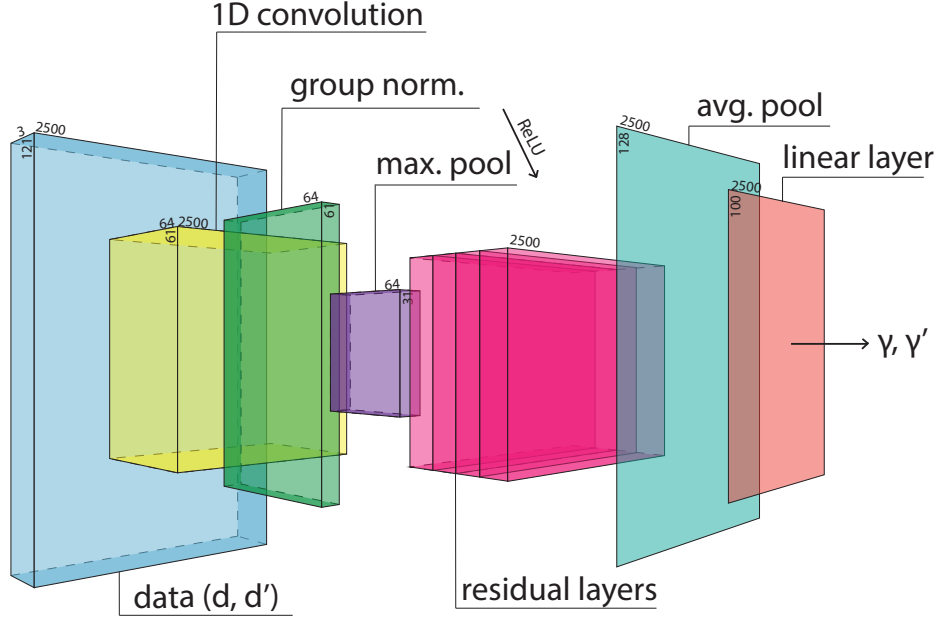


Figure 1. Diagram of the ResNet architecture used for our contraction network, f . We utilize the original light curve data, d , and an augmented version, d' , where the time of arrival and luminosity distance are shifted according to the priors in Table 1. Data d and d' are separately processed through f to obtain γ and γ' as the initial step of our embedding network Γ . This enables a mapping of physical parameters while marginalizing time and distance.

3.1 Data Summary

In order to perform LFI using normalizing flows, we choose parameters $\theta_i \sim p(\theta)$, and simulate light curves \mathbf{d}_i . The pairs $\{\theta_i, \mathbf{d}_i\}$ are used to learn the posterior directly by maximizing the log-likelihood,

$$\log \mathcal{L} = \sum_i p(\theta_i | \mathbf{d}_i). \quad (1)$$

However, a key challenge in implementing LFI on high dimensional data such as light curves is an effective data summary. In this case, we would like to perform inference on the intrinsic parameters, like M_{ej} , V_{ej} , or X_{lan} , even if the data depends on other extrinsic parameters. In the case of a kilonova light curve, signals can be seen as unique if they arrive at different times or occur at different distances, even when the intrinsic parameters of the ejecta are the same. An LFI network unaware of these translations requires the extrinsic parameters of time and distance to be inferred alongside the other physical parameters or marginalized over, leading to a larger, more expensive network. To mitigate the size of the network, we can marginalize over the nuisance parameters by creating an appropriate data summary that preserves the information of only the intrinsic parameters, which are of interest in this case. We utilize self-supervised learning (SSL) to accomplish this goal.

This technique has been used previously in Chatterjee et al. (2023) for simpler, lower dimensional signal morphologies, demonstrating that the creation of an embedding space aids in faster parameter inference. The application of self-supervised learning to create a summary extends to compressing cosmological data and encoding symmetries of partial differential equations as seen in Akhmetzhanova et al. (2024); Mialon et al. (2023). Additionally, self-supervised learning has been used to simplify the complexity of gravitational waves as an initial denoising step (Lin & Kong 2024). Rodrigues & Gramfort (2020) demonstrates a different approach (YuleNet) for data summa-

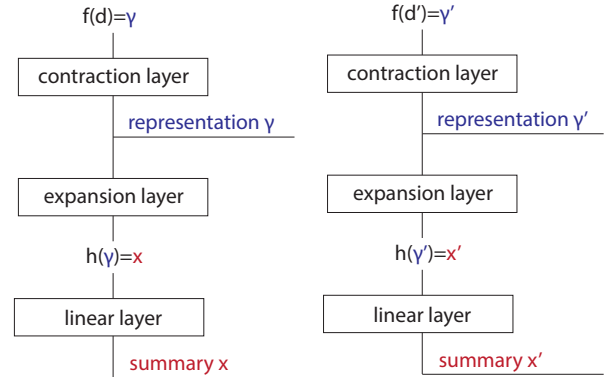


Figure 2. Depiction of our full data summary network. Our data, d and d' are initially passed through the ResNet f . After a contraction layer, we extract the representations γ and γ' . The representation is expanded and passed through the h layer, which is comprised of a linear layer. The output is passed through a final linear layer to output the data summaries, x and x' .

rization for LFI with timeseries data. As a result, we also implement a summarization step for our high-dimensional light curve data.

We create a reduced representation where data with similar intrinsic parameters but different extrinsic parameters are represented in a joint embedding space. This is done by projecting both fixed and shifted data into a 7-dimensional embedding space via a neural network,

$$\Gamma \equiv h \circ f, \quad (2)$$

where f is an adapted ResNet (He et al. 2015), and h is a fully-

connected expander layer. The architecture of f is mapped in Figure 1. Data from the three photometric bands are passed as 3 separate channels to f . We utilize the modifications in Marx et al. (2024) to alter the original ResNet54 architecture, namely the use of 1D convolutions and group normalization in opposition to 2D convolutions and batch normalization. Group normalization acts along the channel dimension, allowing data from all three photometric bands to be processed together. Because the heavy element composition of these light curves greatly influences the color relationship between photometric bands, we prefer the use of group normalization to preserve the color information. We denote this projected space as the data *representation*. The dimensionality of the resulting representation is determined to be 7 through hyperparameter tuning, which is detailed in Section 3.3 and Appendix A.

Our full network architecture is explained in Figure 2's flowchart. After the representation has been extracted, we pass γ and γ' to our 20-dimensional expander layer, h , such that the outputs x, x' are produced:

$$\begin{aligned} \gamma &= f(d) & , & & \gamma' &= f(d'), \\ x &= h(\gamma) & , & & x' &= h(\gamma'). \end{aligned} \quad (3)$$

Here, x and x' represent the data in an embedding space. We call this the data *summary*. To correlate x and x' , we utilize the VICReg loss function (Bardes et al. 2021), which is calculated as a weighted sum:

$$\begin{aligned} L_{VICReg}(x, x') &= \lambda_1 MSE(x, x') + \lambda_2 [\sqrt{Var(x)} + \epsilon \\ &+ \sqrt{Var(x')} + \epsilon] + \lambda_3 [C(x) + C(x')], \end{aligned} \quad (4)$$

where we choose equal weights $\lambda_1 = \lambda_2 = \lambda_3 = 1$ for this study. We minimize the VICReg similarity loss between the embeddings x and x' such that the regularized variance and covariance of the batches are individually reduced, while the invariance between batches is reduced through mean-squared error.

To properly encode the effects of changing t and d_L , we must create two views of the data. We repetitively create 50 light curves using one identical combination of our physical parameters ($\log_{10}(M_{ej}/M_{\odot})$, $\log_{10}(V_{ej}/c)$, and $\log_{10}(X_{lan})$) with unique noise instances. This is done iteratively with novel combinations of the physical parameters to produce a dataset. Each of light curves in this fixed set are positioned at a d_L of 50 Mpc, and start at the same time. Our second data view is created by adjusting t and d_L of each light curve of the fixed set according to the priors listed in Table 1. Our training dataset contains 8,729 unique combinations of M_{ej} , V_{ej} , and X_{lan} , resulting in 872,900 total light curves. The data representation, γ , is trained jointly using these sets of fixed and shifted light curves. 10 minutes of processing time is required to train the network for 50 epochs on one NVidia V100 GPU.

Figure 3 displays the representation γ' for four combinations of physical injection parameters to showcase various areas of the prior selection. We observe that after training, light curves of different $\log_{10}(M_{ej}/M_{\odot})$, $\log_{10}(V_{ej}/c)$, and $\log_{10}(X_{lan})$ are clustered together even with different values of t and d_L , indicating that the two invariant parameters have been successfully marginalized. We utilize the data summarization network as a step in our normalizing flows training.

3.2 Normalizing Flows

For our LFI, we leverage normalizing flows, which transform a simple initial density into a complex distribution by composing a series of learnable transformations (Jimenez Rezende & Mohamed 2015; Durkan et al. 2020). We use a three-dimensional standard normal base distribution and Masked Affine Autoregressive Transforms to compose the normalizing flow, as this transformation only requires one forward pass calculation to evaluate the density (Papamakarios et al. 2017). The LFI is conditioned with the *representation*, $f(d)$, from Eq. (3) and trained by maximizing the log-likelihood with an Adam optimizer. We halve the learning rate when the loss plateaus with a patience of 2 epochs to avoid stagnation.

Only the shifted view is utilized to train the normalizing flow. 472,300 shifted light curves with unique noise and unique combinations of all 5 parameters from Table 1 comprise the training dataset. Hence, this method is suited to the realistic scenario where there is uncertainty in the arrival time, or the distance to the source is not known precisely. The representation, $f(d)$, ensures that this uncertainty is marginalized over. Our best performing model is composed of 9 blocks, 5 transforms, and 90 hidden layers, selected by hyperparameter tuning (see Section 3.3).

The loss curves displayed in Figure 4 demonstrate the negative log probability of several embedding states, all utilizing a fixed batch size of 25, learning rate of 0.0000921, and the same training dataset. The learning rate, batch size, and configurable model parameters are determined through hyperparameter tuning. See Section 3.3 and Appendix A. The frozen case accepts a preconditioned embedding and freezes the weights, while the unfrozen case allows all parameters of the embedding to vary with the flow. For the partially frozen case, we only freeze the weights of the h layer. We investigate the effect of tuning the embedding alongside the flow and find similar rates of convergence. This allows us to select a lighter model with fewer than 1 million configurable parameters. On the other hand, an untrained representation initialized with random weights converges slower. We conclude that the embedding is a valuable step in marginalizing the time and distance values and reducing the overall size of the model. For a model size of $\sim 800,000$ parameters, training requires 50 minutes to train for 100 epochs on one NVidia V100 GPU.

We reserve a small sample of 100 light curves for testing the flow and PyMultiNest. 100 posteriors are drawn from the trained flow for each light curve, and we calculate fraction of events that lie within the credible interval. This is plotted in Figure 4, where we see that the test cases all lie within the credible 3σ bands. Our model consistently returns accurate inferences for all three parameters. Section 4 further discusses the resulting posteriors from PyMultiNest and the flow.

3.3 Hyperparameter Tuning

To achieve optimal configurations of network parameters, hyperparameter tuning is implemented. We utilize the ray.tune Python package to determine batch sizes and learning rates for our training loops, as well as find ideal configurations of our model parameters (Liaw et al. 2018). We searched over 100 combinations of potential dimensionality, kernel sizes, number of h layers, number of blocks, and number of final dimensions for our representation network Γ for a maximum of 50 epochs, or steps. Similarly, we searched through 100 combinations of number of transforms, blocks, and hidden features for the normalizing flow over a maximum of 100 steps. The choices we used are displayed in Table 2, where options in square brackets are discrete and those in parenthesis are continuous. We use

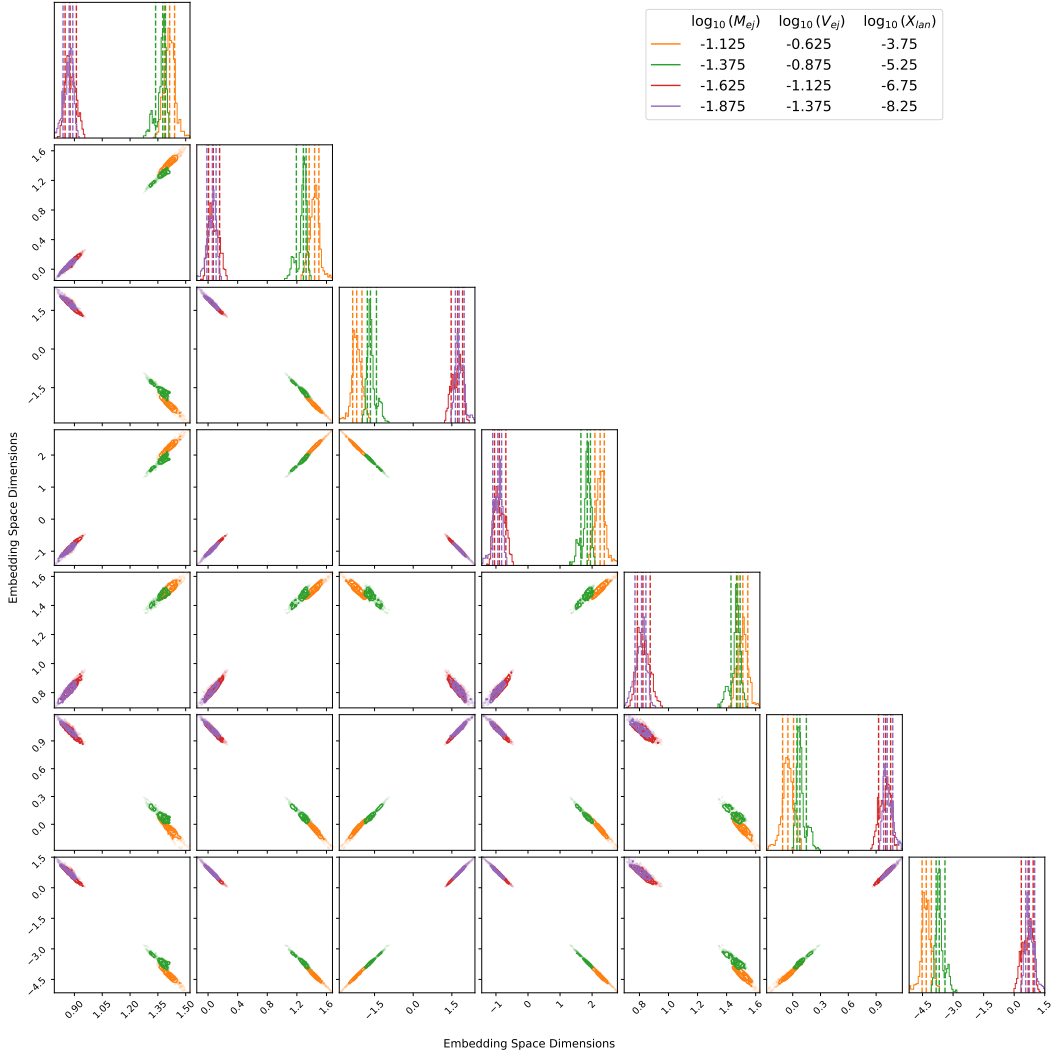


Figure 3. In this figure, we see four combinations of $\log_{10}(M_{ej}/M_{\odot})$, $\log_{10}(V_{ej}/c)$, and $\log_{10}(X_{lan})$ plotted in orange, green, red, and purple. Each set contains 1000 light curves that have been shifted in time and distance. We observe that irrespective of their time and distance, the light curves are clustered with those that share the same $\log_{10}(M_{ej}/M_{\odot})$, $\log_{10}(V_{ej}/c)$, and $\log_{10}(X_{lan})$. This indicates that our nuisance parameters (t , d_L) have been marginalized.

the Async HyperBand Scheduler from Ray to terminate unpromising trials in an effort to reduce the required GPU time, and the best run is selected based on the lowest average validation loss achieved. We utilize the informed tuning to finalize our selection of model parameters. See Appendix A for configuration specifics and loss metrics for the top ten hyperparameter trials.

4 RESULTS

Our parameter estimation posteriors are shown in comparison to PyMultiNest inferences in Section 4.1. We also investigate the effect of missing data in Section 4.2, with a continued investigation into a slower cadence scheme in Appendix B. The inference for each pair of fixed and shifted light curves are in agreement with each other and competitive with results through nested sampling.

4.1 Posteriors

We compare the performance of our model to nested sampling via the package PyMultiNest (Buchner et al. 2014). We maintain the same priors used for data generation, shown in Table 1, while generating the posterior plots. As the normalizing flow intrinsically only knows the given data distribution, we expect its estimation to match the data generation priors. To similarly inform PyMultiNest of the distribution, we use the same prior, but allow the parameter search space to remain 10% larger than the original distribution to accommodate values at the edges of our priors. In addition to PyMultiNest, we investigate the posteriors obtained by the sampler dynesty (Speagle 2020) and conclude that the two methods produce equivalent posteriors. We utilize PyMultiNest for our comparison inferences as it operates faster.

We display our comparison of the fixed and shifted posteriors to PyMultiNest sampling in Figure 5 for one example injection of $\log_{10}(M_{ej}/M_{\odot})$, $\log_{10}(V_{ej}/c)$, and $\log_{10}(X_{lan})$. A comparison is also made between a signal at $d_L = 50$ Mpc and one at $d_L = 200$ Mpc, showing the difficulty nested sampling has when the light curve

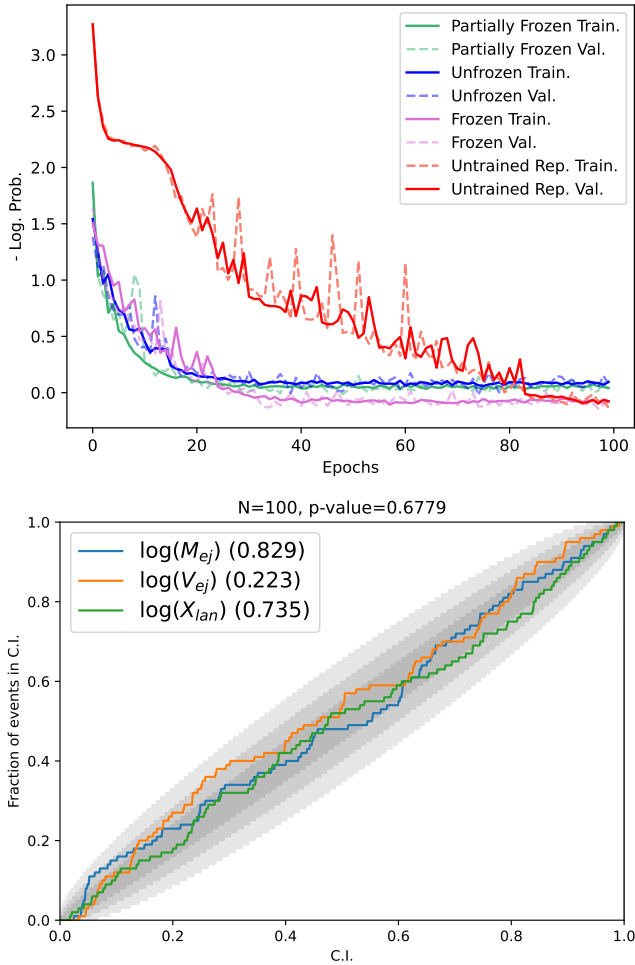


Figure 4. Upper: Training (solid) and validation (dashed) loss curves for variations of the flexibility of the embedding network. The use of an untrained representation is shown in red. The dark blue, light blue, and green curves represent training the flow with a pretrained representation. In dark blue, we allow the representation network to train alongside the flow. In light blue, we allow the parameters in f to train, while the h layer remains fixed. In green, we freeze the weights of the representation network while training the flow. We find that keeping the representation network frozen results in the lowest and fastest convergence. Lower: Percentile-Percentile plots from 100 test light curves, with 1000 posterior samples from each drawn by the flow. The fraction of instances where the parameters lie within the confidence interval is plotted for the three inferred parameters, with M_{ej} in blue, V_{ej} in orange, and X_{Ian} in green. Overlaid are the 1σ , 2σ , and 3σ confidence intervals in decreasing opacity. We find that our samples lie within the confidence intervals, indicating that the correct true parameters are inferred consistently.

peak has shifted significantly. Additionally, distant light curves are dimmer and provide fewer data points for the sampling method to leverage. Our LFI method remains invariant time, as displayed by the complete overlapping of the fixed and the shifted posteriors. The distributions of the flow posteriors also remain consistent for both luminosity distances, demonstrating distance invariance.

To create a statistical sample of posteriors, we draw 100 combinations of our injection parameters from our uniform data distribution which serve as our test set. The light curve data is passed to PyMultiNest, which uses 2048 live points to sample a posterior result. We obtain posteriors from the flow utilizing the identical

Table 2. We select parameter spaces over which we use Ray to search for the best configuration for our models. Below shows the possible options for the representation network and for the flow.

Model	Parameter	Options
Representation	Dimensions	[3, 4, 5, 7, 8]
	Kernel Size	[5, 7, 9, 13]
	h Layers	[1, 2, 3]
	Blocks	[3, 4, 5, 6]
	Final Dimension	[2, 5, 10]
	Batch Size	[25, 50, 75]
	Learning Rate	LogUniform(1×10^{-6} , 1×10^{-4})
Flow	Blocks	[4, 5, 6, 7, 8, 9]
	Transforms	[5, 6, 7, 8, 9, 10]
	Hidden Features	[60, 70, 80, 90, 100]
	Batch Size	[25, 50, 100]
	Learning Rate	LogUniform(1×10^{-6} , 1×10^{-4})

set of shifted light curves. The resulting estimates are compared for our three parameters of interest in Figure 6. We observe that the flow performs well for $\log_{10}(V_{ej}/c)$ and $\log_{10}(M_{ej}/M_{\odot})$, while the inference for $\log_{10}(X_{Ian})$ is challenging. We expect to see a linear correlation between the true values and the inferences. In the case of $\log_{10}(X_{Ian})$, the posterior is uninformative. We find that for all three parameters, the flow returns values within the true distribution found in the data, though the margin of error can lie outside of the true distribution. For PyMultiNest, $\log_{10}(V_{ej}/c)$ remains a difficult parameter to constrain within the given data distribution. We notice similar behavior for $\log_{10}(X_{Ian})$. In these cases, the nested sampler is unable to find the correct minima associated with the true parameter. We observe that the precision and accuracy of the two methods are therefore comparable for $\log_{10}(M_{ej}/M_{\odot})$. The flow has improved accuracy for $\log_{10}(V_{ej}/c)$, but cannot sufficiently provide reliable information for $\log_{10}(X_{Ian})$.

4.2 Model Resilience

Though our model has the ability to infer parameters for a wide variety of kilonova light curves, our training dataset is limited by its regular cadence. To relax the requirement for rapid detections, we chose a cadence of six hours. Based on the recommendation of a rapid cadence between 40 seconds to 30 minutes for transient science from the LSST Science Requirements Document, our cadence selection is reasonable for kilonova detection (Jones et al. 2021). However, we can leverage interpolation to test our model’s resilience to missing or slowly sampled data.

We investigate the results of interpolation to generate missing sections of data by removing four consecutive data points from each band near the peak and performing a linear interpolation over a 36 hour time span. The posteriors for the original light curve and the interpolated one are well aligned. A sample case is displayed in Figure 7 with the interpolated light curve shown on the left, and the posterior in purple overlaid with the posterior from the original light curve on the right. The two posteriors are well aligned, providing a good indication that linear interpolation can be sufficient when the data has missing values. Data can also be interpolated through the use of transformers to achieve uniform cadences from non-uniform detections in the case where linear interpolation is not adequate (Mishra-Sharma 2024).

For further tests in lower cadence regimes, see Appendix B for details on using interpolation to enhance the rapidity of the cadence.

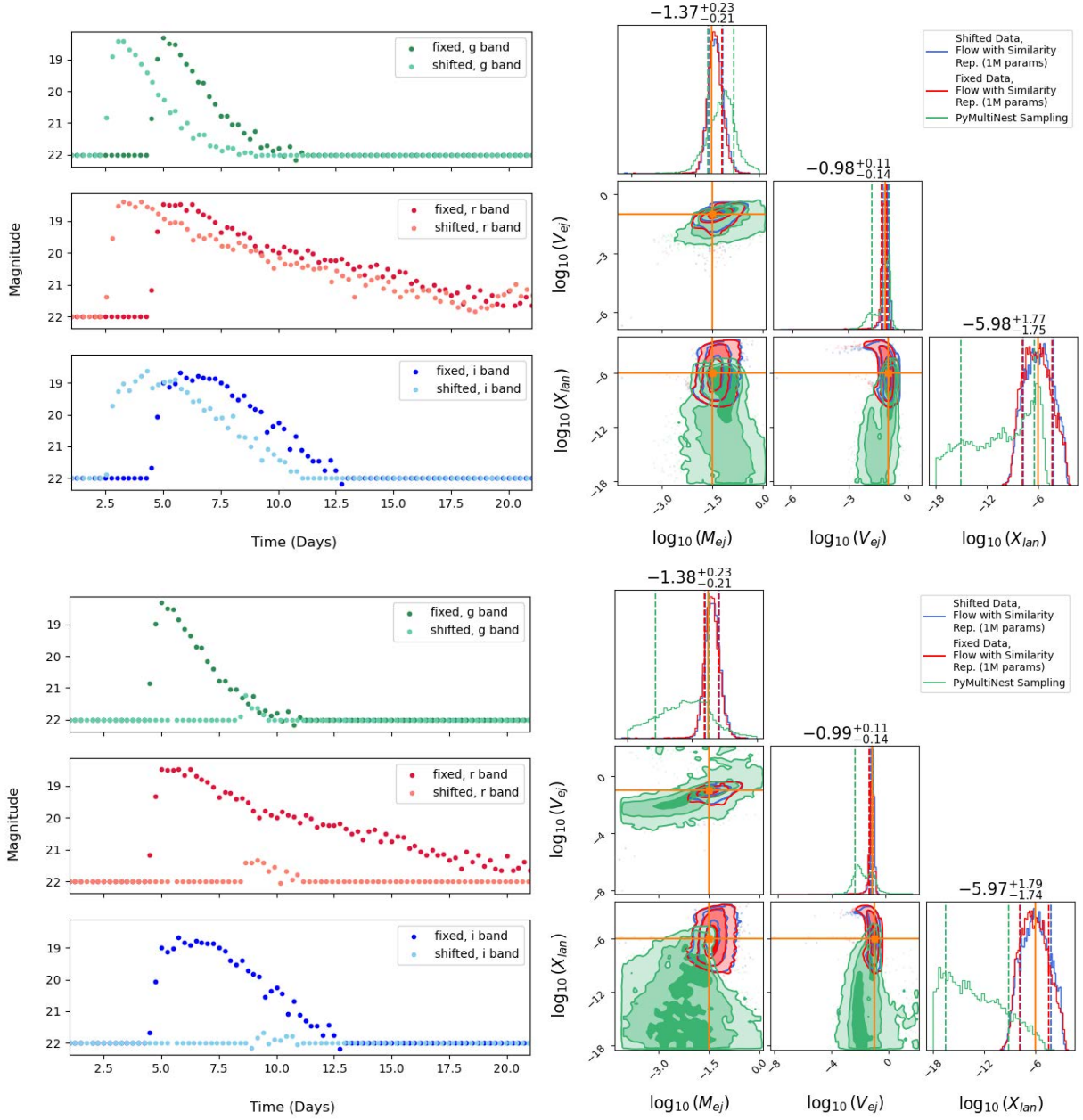


Figure 5. Left panels: Fixed and shifted light curves for injection parameters of $\log_{10}(M_{ej}/M_{\odot}) = -1.5$, $\log_{10}(V_{ej}/c) = -1.0$, $\log_{10}(X_{lan}) = -6$. Upper left: Shifted light curve with $d_L = 50$ Mpc. Bottom left: Shifted light curve with $d_L = 200$ Mpc. Right panels: Corresponding posterior distributions with the shifted light curve posterior from the flow shown in red, its corresponding fixed counterpart inferred from the flow shown in blue, and a comparison to PyMultiNest shown in green. We see agreement between the fixed and shifted posteriors from the flow, and that the three inferred parameters are in agreement with the truth. For M_{ej} , we find similar constraints when comparing to PyMultiNest, but the flow further constrains V_{ej} and X_{lan} .

We expect that observational light curve data will be observed at a non-uniform cadence, and it is possible that key points near the peak will go undetected. Our framework is capable of leveraging interpolation to produce a reliable parameter estimate.

5 CONCLUSION

We present a method to perform parameter estimation on kilonova lightcurves using LFI. Our framework provides a parameter estimation method competitive with pre-existing samplers. We demonstrate that self-supervised learning successfully marginalizes our invariant

parameters of distance and time, decreases the dimensionality of our light curve data, and allows the normalizing flow to converge faster. We do note that our method can be improved in respect to estimating X_{lan} , which can be difficult to inference when distance is marginalized.

Missing data is a common problem that can limit many ML approaches to classification and inference. We demonstrate that for a full day of missing data, our model returns statistically similar inferences when linear interpolation is applied. Additionally, our model provides posteriors in under a second while PyMultiNest requires time on the order of minutes. This allows our model to be a viable

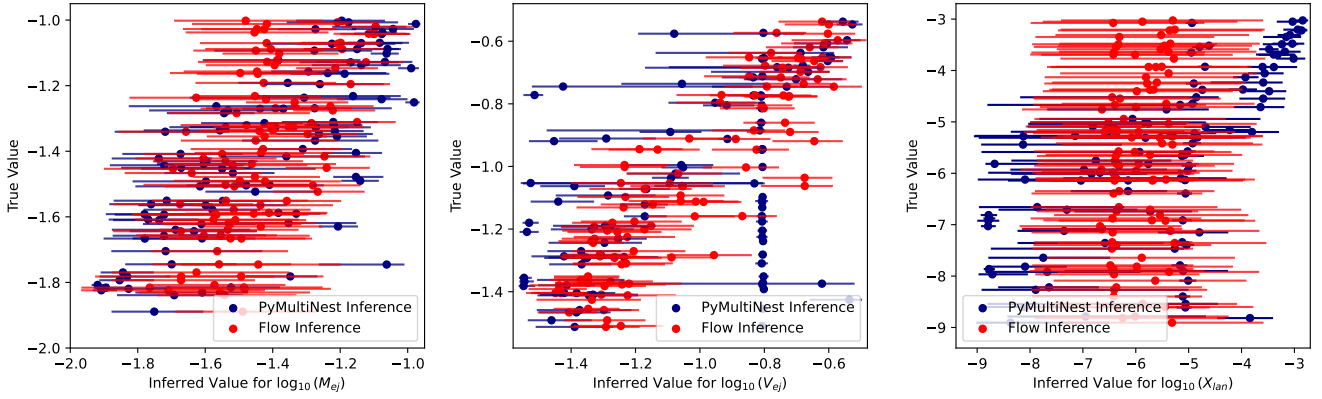


Figure 6. Plotted are 100 inferences and errors for M_{ej} , V_{ej} , and X_{lan} from PyMultiNest in blue, and values from the normalizing flow in red. The inferred values of the parameter estimation methods are plotted against the true value of the parameter. We expect to see a linear pattern when estimation is accurate, as the inference will match the truth. Our model performs well for the quantities $\log_{10}(M_{ej})$ and $\log_{10}(V_{ej})$, but is uninformative for $\log_{10}(X_{lan})$. PyMultiNest has occasional difficulties in constraining a value for $\log_{10}(V_{ej})$ and $\log_{10}(X_{lan})$ for the provided distributions. We utilize the identical shifted light curve sample used in the percentile-percentile plot in Figure 4 for these inferences.

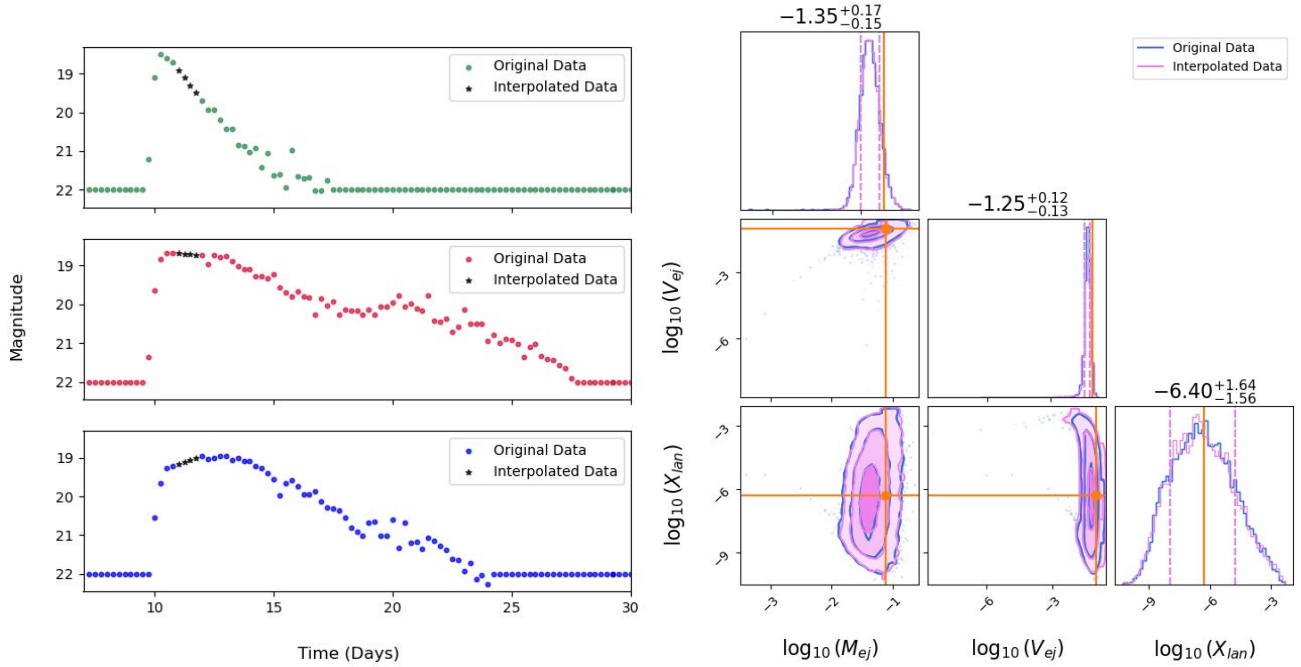


Figure 7. Left: Original light curve data plotted in color with the interpolated points plotted as black stars for all three ZTF bands. Right: Posteriors for a light curve with $\log_{10}(M_{ej}/M_{\odot}) = -1.1045$, $\log_{10}(V_{ej}/c) = -1.0095$, and $\log_{10}(X_{lan}) = -6.2940$. Blue represents the flow results on the original data, and purple with four consecutive data points interpolated. The two posteriors overlap, indicating that interpolating these missing values has little effect on the resulting distribution.

alternative inference method that has the added benefit of time and distance invariance.

Our method is constrained by the choice of kilonova model. In general, light curve models are parametrized by different physical inputs. For example, the model described in Bulla (2023) allows for priors on wind, inclination angle, and electron fraction of the neutron stars in addition to the ejecta mass and velocity parameters found in the Ka2017 model. Including these physical parameters requires retraining and slight restructuring to our network. However, the approach remains consistent regardless of model choice.

Similarly, our model is fine-tuned for ZTF bands g, r, and i. The model requires information for at least one of these bands, but can

be retrained for any number of bands from any instruments provided that the corresponding data can be simulated. As we transition between instruments for light curve observation, our model remains flexible to training with data from multiple bands. The Vera C. Rubin Observatory currently plans to optimize simultaneous light curve sampling in multiple bands, including g, r, and i bands that largely overlap with ZTF (Ivezic et al. 2019; Bellm et al. 2019). Multiple filters can be added or removed by changing the number of data channels supplied to our data summary, Γ . Through a retraining of the model, our framework can be utilized for any instrument.

The use of self-supervised learning as a summarization technique and normalizing flows to perform LFI can also be applied to other

light curve data. Previous work has investigated the role of machine learning techniques on supernova light curves. For example, the Superphot+ classifier uses a gradient-boosted machine architecture to assign types to ZTF supernova light curves (de Soto et al. 2024). Superphot+ relies on nested sampling to estimate several light curve parameters. With a novel dataset, our architecture could be applied to improve secondary classifiers by providing fast and accurate parameter estimation. Since we demonstrate flexibility in cadences and missing data in Section 4.2 and Appendix B, our framework is capable of being applied to observational data.

Our framework is publicly available and ready to use through the NMMA package. With the given constraints mentioned here, a user can access this inference method through the command line and produce a posterior plot for a given NMMA-generated light curve or injection file. Future work is being done to improve the parameter estimation of our method, and to retrain with a separate light curve simulation models and filters to create a host of network weights that can return posteriors for a broad range of kilonova light curves.

ACKNOWLEDGEMENTS

We thank the NMMA team for their invaluable discussions and suggestions for additional testing of the model framework and the incorporation of the model into the NMMA codebase. We thank Peter Pang for reviewing the code. We thank Ethan Marx, Will Benoit, and Alec Gunny for their helpful comments. This work is supported by NSF HDR Institute Grant PHY-2117997, “Accelerated AI Algorithms for Data-Driven Discovery.”

DATA AVAILABILITY

The data processing code, neural network and normalizing flow code, training code, and model weights are available at: <https://github.com/nuclear-multimessenger-astronomy/nmma>. Through this package, command line inference using LFI is available. The training data is also available for use at: <https://doi.org/10.5281/zenodo.11640528>.

REFERENCES

- Abbott B. P., et al., 2017, *Physical Review Letters*, 119, 161101
 Abbott B. P., et al., 2018, *Living Reviews in Relativity*, 21, 3
 Akhmetzhanova A., Mishra-Sharma S., Dvorkin C., 2024, *MNRAS*, 527, 7459
 Almualla M., et al., 2021, *MNRAS*, 504, 2822
 Anand S., et al., 2021, *Nature Astronomy*, 5, 46
 Anand S., et al., 2023, *arXiv e-prints*, p. arXiv:2307.11080
 Andreoni I., et al., 2019, *PASP*, 131, 068004
 Andreoni I., et al., 2022, *ApJS*, 258, 5
 Andreoni I., et al., 2024, *Astroparticle Physics*, 155, 102904
 Bardes A., Ponce J., LeCun Y., 2021, *arXiv e-prints*, p. arXiv:2105.04906
 Bellm E. C., et al., 2018, *Publications of the Astronomical Society of the Pacific*, 131, 018002
 Bellm E. C., et al., 2019, *PASP*, 131, 018002
 Buchner J., et al., 2014, *A&A*, 564, A125
 Bulla M., 2019, *MNRAS*, 489, 5037
 Bulla M., 2023, *MNRAS*, 520, 2558
 Bulla M., Coughlin M. W., Dhawan S., Dietrich T., 2022, *Universe*, 8, 289
 Chatterjee D., Harris P. C., Goel M., Desai M., Coughlin M. W., Katsavounidis E., 2023, *arXiv e-prints*, p. arXiv:2312.07615
 Cowperthwaite P. S., Villar V. A., Scolnic D. M., Berger E., 2019, *ApJ*, 874, 88

- Cranmer K., Brehmer J., Louppe G., 2020, *Proceedings of the National Academy of Science*, 117, 30055
 Dietrich T., Coughlin M. W., Pang P. T. H., Bulla M., Heinzel J., Issa L., Tews I., Antier S., 2020, *Science*, 370, 1450
 Durkan C., Bekasov A., Murray I., Papamakarios G., 2020, nflows: normalizing flows in PyTorch, doi:10.5281/zenodo.4296287, <https://doi.org/10.5281/zenodo.4296287>
 Eichler D., Livio M., Piran T., Schramm D. N., 1989, *Nature*, 340, 126
 Feroz F., Hobson M. P., Bridges M., 2009, *MNRAS*, 398, 1601
 Freiburghaus C., Rosswog S., Thielemann F. K., 1999, *ApJ*, 525, L121
 Frostig D., et al., 2022, *ApJ*, 926, 152
 Gompertz B. P., Nicholl M., Smith J. C., Harisankar S., Pratten G., Schmidt P., Smith G. P., 2023, *MNRAS*, 526, 4585
 Gupta I., Borhanian S., Dhani A., Chattopadhyay D., Kashyap R., Villar V. A., Sathyaprakash B. S., 2023, *Phys. Rev. D*, 107, 124007
 He K., Zhang X., Ren S., Sun J., 2015, *arXiv e-prints*, p. arXiv:1512.03385
 Ivezić Ž., et al., 2019, *ApJ*, 873, 111
 Jimenez Rezende D., Mohamed S., 2015, *arXiv e-prints*, p. arXiv:1505.05770
 Jones R. L., Yoachim P., Ivezić Ž., Neilsen E. H., Riveiro T., 2021
 Kasen D., Metzger B., Barnes J., Quataert E., Ramirez-Ruiz E., 2017, *Nature*, 551, 80
 Kedia A., et al., 2023, *Physical Review Research*, 5, 013168
 Lattimer J. M., Schramm D. N., 1974, *ApJ*, 192, L145
 Li L.-X., Paczyński B., 1998, *ApJ*, 507, L59
 Li L., Jamieson K., Rostamizadeh A., Gonina K., Hardt M., Recht B., Talwalkar A., 2018, Massively Parallel Hyperparameter Tuning, <https://openreview.net/forum?id=S1Y7001RZ>
 Liaw R., Liang E., Nishihara R., Moritz P., Gonzalez J. E., Stoica I., 2018, *arXiv preprint arXiv:1807.05118*
 Lin Y.-C., Kong A. K. H., 2024, *arXiv e-prints*, p. arXiv:2403.04350
 Martin D., Perego A., Arcones A., Thielemann F. K., Korobkin O., Rosswog S., 2015, *ApJ*, 813, 2
 Marx E., et al., 2024, *arXiv e-prints*, p. arXiv:2403.18661
 Mathias L. W. P., Di Clemente F., Bulla M., Alessandro D., 2024, *MNRAS*, 527, 11053
 Metzger B. D., 2017, *Living Reviews in Relativity*, 20, 3
 Mialon G., et al., 2023, *arXiv e-prints*, p. arXiv:2302.07842
 Mishra-Sharma S., 2024, Generative Spectra Lightcurves, <https://github.com/smsharma/generative-spectra-lightcurves>
 Pang P. T. H., et al., 2023, *Nature Communications*, 14, 8352
 Pang P. T. H., et al., 2024, NMMA: Nuclear Multi Messenger Astronomy framework, Astrophysics Source Code Library, record ascl:2402.001
 Papamakarios G., Pavlakou T., Murray I., 2017, *arXiv e-prints*, p. arXiv:1705.07057
 Peng Y., et al., 2024, *arXiv e-prints*, p. arXiv:2402.05871
 Radice D., Perego A., Zappa F., Bernuzzi S., 2018, *ApJ*, 852, L29
 Rodrigues P. L. C., Gramfort A., 2020, *arXiv e-prints*, p. arXiv:2012.02807
 Sagués Carracedo A., Bulla M., Feindt U., Goobar A., 2021, *MNRAS*, 504, 1294
 Saha S., et al., 2024, *ApJ*, 961, 165
 Siegel D. M., 2019, *European Physical Journal A*, 55, 203
 Skilling J., 2006, *Bayesian Analysis*, 1, 833
 Speagle J. S., 2020, *MNRAS*, 493, 3132
 Tanvir N. R., et al., 2017, *ApJ*, 848, L27
 Wollaeger R. T., et al., 2021, *ApJ*, 918, 10
 Zhu Y. L., Lund K. A., Barnes J., Sprouse T. M., Vassh N., McLaughlin G. C., Mumpower M. R., Surman R., 2021, *ApJ*, 906, 94
 de Soto K. M., et al., 2024, *arXiv e-prints*, p. arXiv:2403.07975

APPENDIX A: HYPERPARAMETER TUNING

Tables A1 and A2 display the ten best hyperparameter tuned runs for the embedding network and the normalizing flow. Trial 2 and Trial 40 are selected as the respective best trials based on the lowest validation loss achieved at the termination of the run. These runs are shown in figure A1, which displays the training loss curves for the

Table A1. Ten best hyperparameter tuning configurations for the similarity embedding parameters.

Trial	Dimensions	Kernel Size	h Layers	Blocks	Final Dimension	Batch Size	Learning Rate	Final Train Loss	Final Val. Loss
2	7	5	1	4	5	50	2.75e-05	0.01502	0.01172
3	7	7	1	4	5	25	1.32e-05	0.03583	0.12160
7	5	7	3	6	2	25	3.51e-05	0.02391	0.02914
10	8	7	1	6	2	25	2.64e-05	0.01324	0.03076
11	5	5	1	3	2	25	4.31e-06	0.02485	0.13644
17	5	9	1	5	2	25	1.67e-05	0.01662	0.13725
31	5	7	2	6	2	25	4.71e-06	0.01231	0.02960
40	8	9	2	3	2	50	2.39e-05	0.04336	0.05734
48	8	9	1	5	2	50	8.60e-05	0.01128	0.02089
98	4	7	1	4	5	50	1.13e-06	0.05847	0.10924

Table A2. Ten best hyperparameter tuning configurations for the normalizing flow parameters.

Trial	Blocks	Transforms	Hidden Features	Batch Size	Learning Rate	Final Train Loss	Final Val. Loss
0	8	5	100	100	6.39e-05	0.58579	0.55771
4	10	4	100	25	3.38e-05	0.56152	0.60114
11	9	7	80	25	4.09e-05	0.65374	0.72734
19	6	5	70	25	4.05e-05	0.71651	0.82130
28	10	6	100	25	8.76e-05	0.34584	0.33634
40	9	5	90	25	9.12e-05	0.09280	-0.18805
57	6	5	90	25	9.28e-05	0.37192	0.53521
65	9	6	70	25	3.82e-05	0.79535	0.90459
75	10	7	70	25	6.89e-5	0.37713	0.40245
98	9	6	80	25	9.33e-05	0.12195	0.04436

ten best trials for the embedding and for the normalizing flow. To increase the efficiency of hyperparameter searches, we leverage the Async HyperBand Scheduler (ASHA) from Ray. This scheduling algorithm uses the user-selected optimization metric (here, minimizing the validation loss) to identify poorly performing runs and terminate them early (Li et al. 2018). In this way, we can efficiently search over the parameter spaces in Table 2 for our models.

APPENDIX B: MODEL RESILIENCE

As we intend for our framework to be used with a variety of optical instruments, it is imperative that the model can adjust to several cadences. For our first test, we discard every other detection and interpolate new data points in their stead. Again, we find that the model has sufficient information to generate an inference with high accuracy. Figure B1 displays a sample posterior in yellow alongside its respective light curve with the interpolated values. We observe alignment between the two.

This test indicates that our model has enough flexibility to accommodate different observational cadences to perform accurate parameter estimation.

This paper has been typeset from a $\text{\TeX}/\text{\LaTeX}$ file prepared by the author.

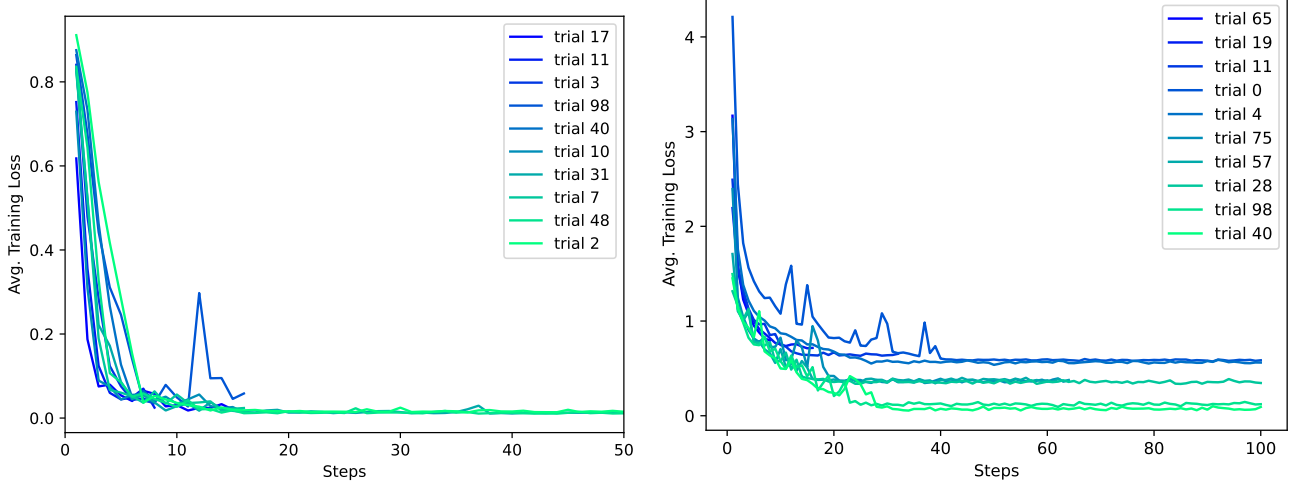


Figure A1. Training loss curves for the 10 best configurations of the embedding network (upper) and the normalizing flow (lower). We utilize the configurations of the network parameters selected in trial 2 and trial 40 for our models as they converge to the lowest training and validation loss.

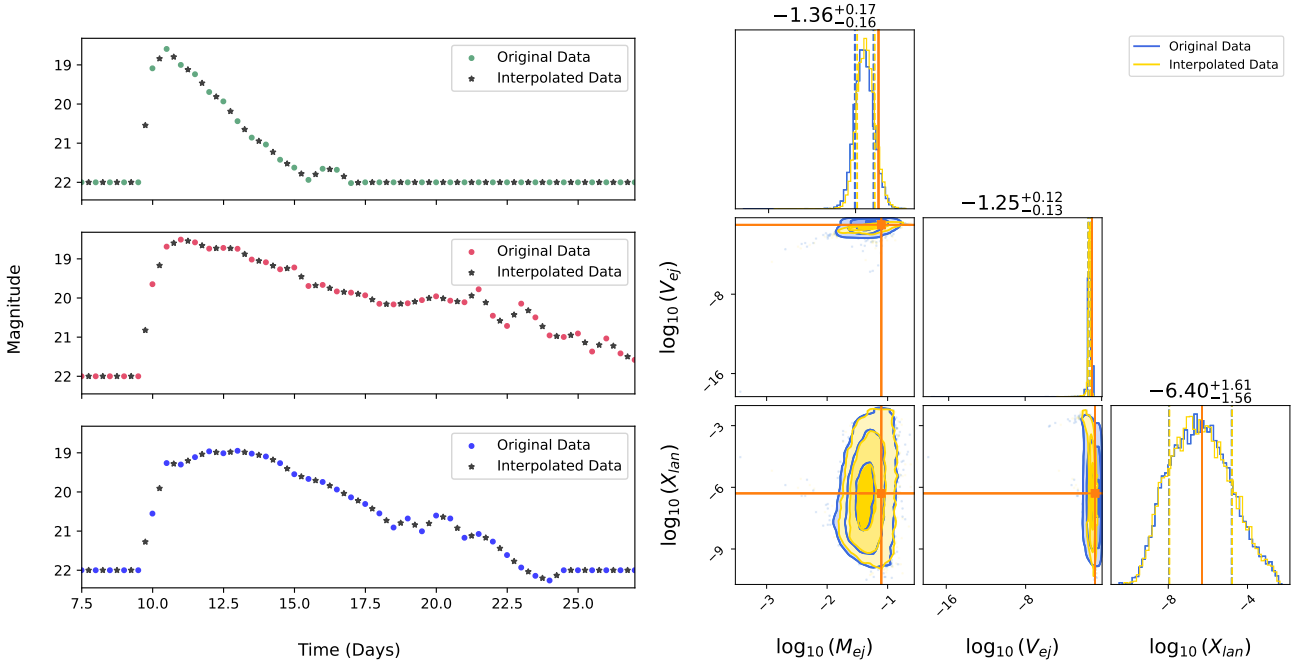


Figure B1. Left: Original light curve data plotted in color with the interpolated points plotted as black stars for all three ZTF bands. Right: Posteriors for a light curve with $\log_{10}(M_{ej}/M_{\odot}) = -1.1045$, $\log_{10}(V_{ej}/c) = -1.0095$, and $\log_{10}(X_{lan}) = -6.2940$. Blue represents the flow results on the original data, and yellow with every other data point interpolated. The two posteriors overlap, indicating that interpolating these missing values has little effect on the resulting distribution.